Redox-Dependent Structural Changes in the *Azotobacter vinelandii* Bacterioferritin: New Insights into the Ferroxidase and Iron Transport Mechanism[†,‡]

Larkin Swartz,[§] Mike Kuchinskas,[||] Huiying Li,[||] Thomas L. Poulos,[||] and William N. Lanzilotta*[,§]

Department of Molecular Biology and Biochemistry, University of California, Irvine, California 92697, and Department of Biochemistry and Molecular Biology, University of Georgia, Athens, Georgia 30602

Received January 23, 2006; Revised Manuscript Received February 20, 2006

ABSTRACT: In this work, we report the X-ray crystal structure of the aerobically isolated (oxidized) and the anaerobic dithionite-reduced (at pH 8.0) forms of the native *Azotobacter vinelandii* bacterioferritin to 2.7 and 2.0 Å resolution, respectively. Iron K-edge multiple anomalous dispersion (MAD) experiments unequivocally identified the presence of three independent iron-containing sites within the protein structure. Specifically, a dinuclear (ferroxidase) site, a *b*-type heme site, and the binding of a single iron atom at the four-fold molecular axis of the protein shell were observed. In addition to the novel observation of iron at the four-fold pore, these data also reveal that the oxidized form of the protein has a symmetrical ferroxidase site containing two five-coordinate iron atoms. Each iron atom is ligated by four carboxylate oxygen atoms and a single histidyl nitrogen atom. A single water molecule is found within hydrogen bonding distance of the ferroxidase site that bridges the two iron atoms on the side opposite the histidine ligands. Chemical reduction of the protein under anaerobic conditions results in an increase in the average Fe−Fe distance in the ferroxidase site from ∼3.5 to ∼4.0 Å and the loss of one of the ligands, H130. In addition, there is significant movement of the bridging water molecule and several other amino acid side chains in the vicinity of the ferroxidase site and along the D helix to the three-fold symmetry axis. In contrast to previous work, the higher-resolution data for the dithionite-reduced structure suggest that the heme may be bound in multiple conformations. Taken together, these data allow a molecular movie of the ferroxidase gating mechanism to be developed and provide further insight into the iron uptake and/or release and mineralization mechanism of bacterioferritins in general.

Ferritins are iron storage proteins that are found in essentially all forms of life. Not too surprisingly, these ubiquitous proteins have a conserved structure that is generally described as a spherical shell composed of 24 individual protein monomers (*1*, *2*). Up to 4500 iron atoms can be stored in the nanostructure formed by the polypeptide sphere. In addition to an essential role in iron storage for key cofactors in respiration, photosynthesis, nitrogen fixation, and DNA synthesis, smaller ferritin-like proteins have also been implicated in DNA protection during cell starvation (also known as Dps proteins). The essential nature of ferritins is further underscored by the increased sensitivity to oxidative stress and lethality of gene deletion (*3*−*7*). In addition, ferritin and ferritin-associated proteins have also been implicated in the efficient host colonization of certain opportunistic bacteria (*8*).

All ferritins store the iron atoms within the core of the peptide sphere that is approximately 8 nm in diameter (for the 24-mer) and is lined with a phosphate layer in the animal ferritins. Similarly, the bacterioferritins contain a homogeneous phospho-oxy-hydroxide mineral core. A significant difference between the bacterioferritins and the animal ferritins is the subunit composition of the shell structure. While bacterioferritins are composed of a single type of subunit ($M_r \sim 19\,000$), the animal ferritins contain two related subunits termed heavy and light chains. In addition to this distinction, some bacterioferritins also contain a heme *b* cofactor bound at the interface of two monomers. For the bacterioferritins, two identical monomers are related by a *C*2 (180°) rotation axis, and it is the repetition of 12 of these homodimeric units that make up the protein shell. Both the heavy chain of the animal ferritin and the bacterioferritin monomer contain a ferroxidase center that catalyzes the oxidation of Fe^{2+} by molecular oxygen (O_2). A dinuclear iron site is at the heart of the ferroxidase reaction and is built upon a highly conserved ligand environment buried within the hydrophobic core of a four-helix bundle. Given the role of ferritins in coupling the energy of iron oxidation by O_2 to the storage of large amounts of iron under physiological conditions, it is not surprising that this ligand architecture is also observed in other non-heme diiron-containing proteins involved in oxygen transfer, as well as oxidative stress protection and O_2 activation (*9*, *10*).

The deposition of iron into the ferritin and bacterioferritin core has been well studied and appears to proceed by O_2-

[†] This work was supported by a grant from the American Heart Association to W.N.L. (AHA 0465228B) and NSF Grant MCB0315283 to T.L.P.

[‡] Atomic coordinates for the oxidized and anaerobic dithionite-reduced structures have been deposited in the Protein Data Bank as entries 2FL0 and 2FKZ, respectively.

* To whom correspondence should be addressed. Phone: (706) 542-1324. Fax: (706) 542-1738. E-mail: wlanzilo@bmb.uga.edu.

[§] University of Georgia.

[||] University of California.

10.1021/bi060146w CCC: $33.50
Published on Web 03/16/2006

dependent oxidation of ferrous iron. For ferritin, this has been shown to occur via a diferric peroxo (DFP) intermediate to form diferric oxo complex precursors of the hydrated ferric oxide mineral (*11*−*14*). However, a distinct discrepancy exists between the bacterioferritins and the ferritins of higher organisms. Extensive kinetic and stoichiometric studies with native horse spleen apoferritin and recombinant heavy chain ferritins have led to the proposal that two limiting Fe^{2+}:O_2 stoichiometries occur during ferritin core reconstitution. These stoichiometries are summarized by reactions 1 and 2 (*11*−*16*).

$$2Fe^{2+} + O_2 + 6H_2O \rightarrow 2Fe(OH)_3 + H_2O_2 + 4H^+ \quad (1)$$

$$4Fe^{2+} + O_2 + 10H_2O \rightarrow 4Fe(OH)_3 + 8H^+ \quad (2)$$

In these reaction schemes, reaction 1 results in the production of H_2O_2 that escapes into the solution surrounding the peptide shell during mineralization of the core. The net result is Fe^{2+}:O_2 ratios close to 2.0 for iron deposition (*15*). In contrast, Fe^{2+}:O_2 ratios of 4.0 suggest that iron incorporation is occurring by reaction of Fe^{2+} and O_2 by reaction 2 (*11*, *14*−*16*). For higher organisms, it has been proposed that initially reaction 1 is catalyzed by the native and recombinant heavy chain ferritins with reaction 2 becoming important once a sufficiently large mineral core has formed (*14*, *15*). This does not seem to be the case for the bacterioferritins (either 12 or 24 subunit types) that appear to reduce O_2 directly to H_2O during iron incorporation (*17*, *18*). This is perplexing, given the remarkably similar structural features of the ferroxidase site in the bacterioferritins and the ferritins from higher organisms. Of specific interest is the observation that *Escherichia coli*, *Listeria innocua*, and *Azotobacter vinelandii* bacterioferritins actually produce H_2O from O_2 reduction during iron deposition (*15*, *17*, *18*). Although transient H_2O_2 formation has been observed for *E. coli* bacterioferritin (EcBF), the peroxide has been predicted to rapidly react with Fe^{2+} to account for Fe^{2+}:O_2 ratios of 4.0 observed for EcBF (*19*) during the mineralization process. Further complicating the bacterioferritin story is the recent report that *A. vinelandii* bacterioferritin (AvBF)[1] also gives Fe^{2+}:O_2 ratios of 4.0 during iron deposition, but without significant formation of H_2O_2 (*15*). The latter observation was rationalized by the observation of similar reaction rates for O_2 and H_2O_2 with the ferroxidase center of AvBF. In any case, this still implies a direct reduction of O_2 by $4Fe^{2+}$ and presents an enigma given the conserved structure of the ferroxidase center.

While the number of ferritins with a known amino acid sequence is staggering, relatively few X-ray crystal structures have been presented, especially for the bacterioferritins. At present, four bacterioferritin structures have been reported from *E. coli* (*20*, *21*), *Rhodobacter capsulatus* (*22*), *Desulfovibrio desulfuricans* (*23*), and *A. vinelandii* (*24*). Of significant interest was the observation that the *A. vinelandii* crystals and subsequent structure were reported to be "accidentally" obtained while attempting to crystallize a Cr-substituted varient of nitrogenase component I (*24*). The resolution of this structure was 2.6 Å, and further spectroscopic characterization of the crystals confirmed that the heme groups of the bacterioferritin were in a ferrous state. The presence of a Ba^{2+} ion at a four-fold channel was observed, and it was further suggested that this channel might provide Fe^{2+} conductivity and selectivity. Liu et al. (*24*) also proposed a dynamic gating mechanism based on the iron occupancy and unique positioning of conserved residues in the ferroxidase center when compared with other known bacterioferritin structures.

To further investigate the hypothesis that redox-dependent structural changes may be part of a gating mechanism, we have determined the crystal structures of AvBF in the aerobic as-isolated (oxidized) and anaerobic dithionite-treated states. Reversible, redox-dependent conformational changes are observed that provide new insight into the iron incorporation−release mechanism. Moreover, the higher resolution of the reduced state also provides more insight into the orientation of the heme at the interface that is in contrast to what was previously reported. Finally, a novel result of the MAD phasing methods employed during structure determination was the identification of iron atoms at the 4-fold axis of the bacterioferritin shell, providing further evidence that these pores might serve a role in ion selectivity by allowing only ferrous ions (or ions of equivalent size) to pass through this pore.

EXPERIMENTAL PROCEDURES

Isolation and Crystallization of A. vinelandii Bacterioferritin. A. vinelandii strain UW3 was grown at 30 °C for 24 h on Burk's medium supplemented with 2.2 g/L ammonium acetate. Isolation of *A. vinelandii* bacterioferritin (AvBF) was performed in a three-step procedure under aerobic conditions. The cells were broken with a French pressure cell at ~16000 psi in 50 mM Tris (pH 8.0). Following centrifugation at 56000*g* to remove the membranes, the DNA was precipitated by addition of poly(ethyleneimine) (PEI) to a concentration of 0.2% (v/v) from a 5% stock solution. The precipitated DNA was centrifuged at 10000*g* for 10 min, and the DNA pellets were saved. The DNA pellets were resuspended in 50 mM Tris (pH 8.0) containing 800 mM NaCl using a tissue homogenizer. This suspension was then centrifuged at 10000*g* to remove the precipitated DNA. The solute was then concentrated and subjected to gel filtration on a calibrated Sephadex S-200 column equilibrated with 25 mM Tris (pH 8.0) containing 250 mM NaCl. Fractions containing AvBF were concentrated in this buffer and then split into two aliquots. One of the aliquots was made anaerobic by several rounds of degassing on an argon manifold prior to crystallization. Crystallization experiments were performed by the capillary batch method under both aerobic and anaerobic conditions with the latter being performed in an atmosphere of 95% nitrogen and 5% hydrogen where the oxygen levels where maintained below 1 ppm at all times. In either case, diffraction-quality crystals appeared within 1 or 2 weeks in mother liquor containing 15% ethanol, 100 mM imidazole, and 200 mM $MgCl_2$. Prior to freezing the crystals for data collection, we increased the concentration of glycerol in steps of 2.5% until a final concentration of 30% was obtained. To further prevent any potential exposure of the anaerobic crystals to oxygen, these crystals were frozen in liquid nitrogen inside the anaerobic chamber and sodium dithionite (final concentration of 2 mM)

[1] Abbreviations: Tris, tris(hydroxymethyl)aminomethane; PEI, poly(ethyleneimine); AvBF, *Azotobacter vinelandii* bacterioferritin; DdBF, *Desulfovibrio desulfuricans* bacterioferritin.

Table 1: Data Collection, Phasing, and Refinement Statistics

	oxidized (OX)	reduced (RED)	anomalous OX	anomalous RED
wavelength (Å)	0.98	0.98	1.63	1.739
resolution range (Å)	50.0−2.7	50.0−2.0	50.0−3.0	50.0−2.82
no. of unique observations	89043	109019	31537	39191
completeness	98.6 (93.0)[a]	99.5 (99.3)[a]	99.9 (99.3)[a]	99.9 (99.9)[a]
R_{sym} (%)[b]	7.6 (28.9)[a]	5.9 (28.5)[a]	6.5 (12.4)[a]	5.2 (26.9)[a]
I/σ	30.1 (6.8)[a]	15.7 (2.8)[a]	32.8 (20.4)[a]	8.1 (4.6)[a]
R_{cullis} (acen/anom)			0.49/0.49	0.57/0.58
phasing power (acen/anom)			0.85/0.86	0.94/0.97
no. of sites			22	22

	oxidized	reduced
unit cell	$a = b = 124.48$ Å, $c = 285.11$ Å	$a = b = 123.67$ Å, $c = 284.27$ Å
no. of protein atoms	10084	10084
no. of solvent atoms	387	785
resolution limits (Å)	50.0−2.7	50.0−2.0
R_{cryst} (%)	20.3	21.6
R_{free} (%)	25.6	24.7
rmsd for bonds (Å)	0.007	0.014
rmsd for angles (deg)	1.14	1.97
average *B* factor (Å^2)	36.46	23.65

[a] Numbers in parentheses correspond to the data in the outermost resolution shell. [b] $R_{sym} = \sum_{hkl}[\sum_I(|I_{hkl,I} - \langle I_{hkl}\rangle|)]/\sum_{hkl,I}\langle I_{hkl}\rangle$, where I_{hkl} is the intensity of an individual measurement of the reflection with indices *hkl* and $\langle I_{hkl}\rangle$ is the mean intensity of that reflection.

was added to the mother liquor 1 h prior to freezing. Given the reduction potentials of diiron sites with structures similar to the ferroxidase site reported here (typically ≥0 mV) (*25*), under these conditions, the heme iron and the iron at the ferroxidase site should be in a ferrous state, while reduction of the mineralized iron in the core will be occurring at a slow rate (*26*).

Data Collection, Phase Determination, Model Building, and Refinement. Data were collected at the Advanced Light Source on beamline 5.0.2. The initial position of the iron atom was identified by MAD phasing methods using space group *R*32 (Table 1). The three-wavelength MAD data were collected at 7.12 (inflection point), 7.13 (peak), and 7.60 keV (remote). In space group *R*32, the asymmetric unit consisted of four monomers. Two of these monomers form a complete homodimer with a *b*-type heme at the interface. However, this also positioned two additional heme groups on a crystallographic two-fold axis. Given the nonsymmetrical nature of the *b*-type heme, it became immediately clear that the correct space group assignment was *R*3. Further model building and phase refinement were therefore carried out in this space group. In this case, the asymmetric unit contains eight monomers and four *b*-type heme groups. The implications of these observations are discussed in the following sections. Initial identification of the iron positions and phase refinement were carried out with SHELXD (*27*) and SOLVE/RESOLVE (*28*, *29*) using a script downloaded from the SSRL webpage (http://smb.stac.stanford.edu/templates/MAD_scripts/). Additional iron atoms were identified by iterative analysis of the anomalous data with ISAS (*30*) in space group *R*3. Model building and further phase refinement were carried out using O (*31*) and CNS (*32*), respectively.

RESULTS AND DISCUSSION

Redox-Dependent Changes in the Ferroxidase Center. At present, only one other native bacterioferritin structure has been reported in a number of oxidation states (*23*), the *D. desulfuricans* bacterioferritin (DdBF). Similar to the results presented here, the data presented by Macedo et al. reported the structure of the aerobic crystals and the impact of chemical reduction under strictly anaerobic conditions. The data for the native (aerobic) AvBF are presented in Figure 1A. For both AvBF and DdBF, a significant amount of bridging density is observed between the two iron atoms in this state. However, unlike what was reported for DdBF, no additional density was observed in the difference ($F_o - F_c$) map when the density was modeled as a single water atom in our data (Figure 1A). This is consistent with the position of this density relative to the two iron atoms (up to 4 Å in some monomers). It is important to point out that even low-dose X-ray data collection can lead to significant reduction of metal centers (*33*), and hence, this may be an underlying factor in the slight differences observed in the bridging density between DdBF and AvBF. In general, however, the oxidized state of the AvBF ferroxidase site observed here is relatively symmetrical with each iron atom ligated by four oxygen atoms from three glutamate residues and a nitrogen atom from the side chain of a single histidine residue. Chemical reduction of the ferroxidase site in AvBF had a significant impact on the structure (Figure 1B). At the heart of these redox-dependent conformational changes is the expansion of the Fe−Fe distance by approximately 0.5 Å. In addition, the iron atom that is ligated by the side chain of H130 loses this histidyl ligand. As can be seen in Figure 1, this side chain moves away from the ferroxidase site upon reduction, a structural change that is not observed in DdBF. The *B* factors for the iron atom associated with this ligand also increase, suggesting that the site may not be fully occupied. Further iterative *B* factor and occupancy refinement of this iron atom resulted in an average occupancy of 0.80, confirming that this may in fact be the case. However, if the occupancy was set to 0.80 for this iron atom, there were no significant improvements in the overall map quality or *R* factors (<0.1%), and therefore, the occupancy was left at 1.0 in the final models. Although the equivilent histidine residue in DdBF (H135) was not observed to move upon reduction, similar changes in the density bridging the iron atoms upon reduction were observed. Specifically, there is a shift in the bridging electron density toward the lower-occpancy iron atom. For DdBF, subsequent exposure of the reduced, dithionite-free, crystals to oxygen resulted in loss of one of the iron atoms (*23*). An interesting observation is that the departing iron atom in DvBF was ligated by H59 (H54 in AvBF). We have collected data on reduced AvBF crystals that were subsequently exposed to oxygen and saw no significant peaks in the difference maps when the oxidized model was used to fit the data, suggesting that the conformational changes observed in AvBF, in contrast to DdBF, are also reversible.

A Redox-Dependent Gating Mechanism in A. vinelandii Ferritin. The idea that a continuous channel for translocation of iron to and from the mineral core might be formed by the concerted movement of two residues on the inner side of the ferroxidase site has been proposed for the bacterioferritins

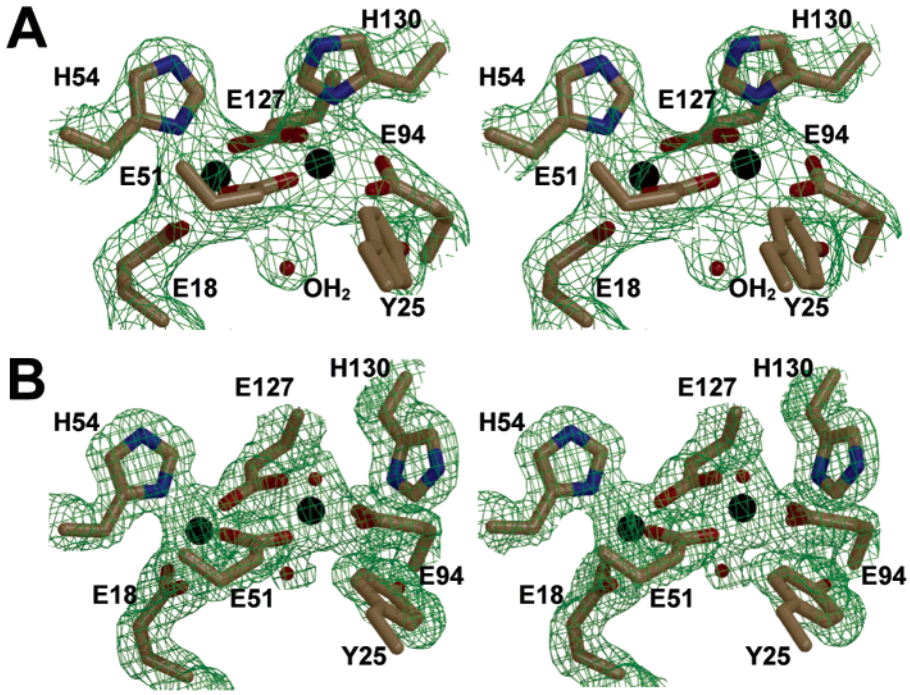

FIGURE 1: Redox-dependent structural changes at the ferroxidase site in *A. vinelandii* bacterioferritin. Wall-eyed stereoview of the molecular model and the $F_o - F_c$ composite omit map generated with the simulated annealing protocol. The composite omit map is represented by the green cage and is shown at 3σ for the oxidized (A) and anaerobic dithionite-treated (B) data. For clarity, the amino acid side chains are labeled for only the oxidized model. Carbon, oxygen, nitrogen, and iron atoms are colored tan, red, blue, and black, respectively.

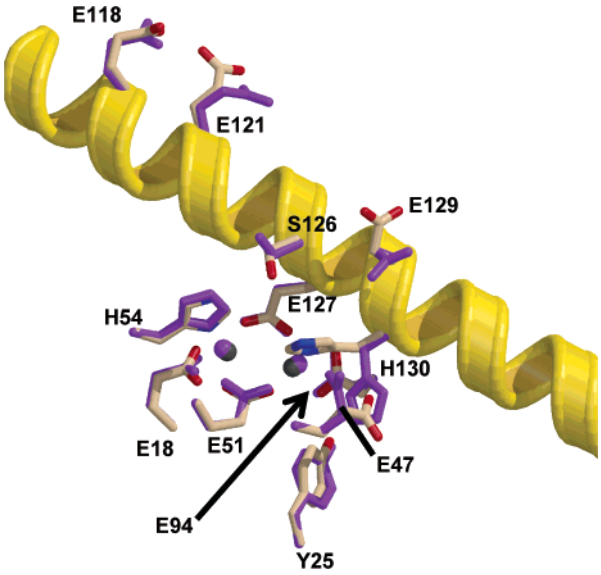

FIGURE 2: Redox-dependent structural changes between the ferroxidase site and the three-fold axis. Structural alignment of the oxidized and anaerobic dithionite-treated models of *A. vinelandii* bacterioferritin. Carbon, oxygen, nitrogen, and iron atoms are colored tan, red, blue, and black, respectively, in the oxidized model. All atoms are colored purple in the anaerobic dithionite-treated model. For reference, the helix from residue 114 to 143 is also colored gold. The side chains of residues E118 and E121 are located in the three-fold pore.

(*23*, *24*). Our results essentially confirm this hypothesis and demonstrate that the side chains of H130 and E47 can serve a gating function by exchanging positions in a redox-dependent manner. The redox-dependent exchange of these two side chains is shown in Figure 2. Figure 2 also shows that, in addition to the movement of H130 and E47, reduction also results in the movement of several side chains between the ferroxidase site and the three-fold axis. Specifically, it is clear that oxidation or reduction of the ferroxidase site results in the movement of polar and negatively charged side chains located along the D helix between the three-fold pore and the ferroxidase site. Of particular interest are residues E118 and E121. These residues are found at a three-fold symmetry axis, resulting in six (two from each monomer) negatively charged side chains at this site. These residues make up the innermost layer of the three-fold pore, and due to the symmetry of this site, the movement of E121 would be amplified 3-fold. This observation is of particular interest given the work presented by Theil and co-workers that suggests the three-fold axis of human ferritin serves as a dynamic aperture that could be controlled by cytoplasmic factors for iron release in vitro (*34*, *35*). Our observations are also of significant interest given the observation by Zeth et al. of biomineralization at the three-fold pore of the *Halobacterium salinarum* DpsA protein (*36*). The redox-dependent movement of these side chains certainly supports the idea of a potential communication/transport pathway between the ferroxidase site and the three-fold molecular axis of the protein shell. A working hypothesis would suggest that diferric peroxo species are translocated to the three-fold axis in the early stages of mineralization for the bacterioferritins and dps proteins. However, aside from the conserved acidic groups (E118 and E121 in AvBF and D131 and E134 in human ferritin), the general features of the three-fold pore are notably different in AvBF, and bacterioferritins in general, when compared with the ferritins of higher organisms such as humans. In the latter case, these acidic side chains are the only barrier for ion transport across the three-fold pore. In AvBF, as is the case with most bacterioferritins, the three-fold pore has three layers consisting of an inner and middle layer of acidic residues and an outer layer of positive charge (*2*). The middle and outer layer of the three-fold pore of the bacterioferritins are actually formed by an

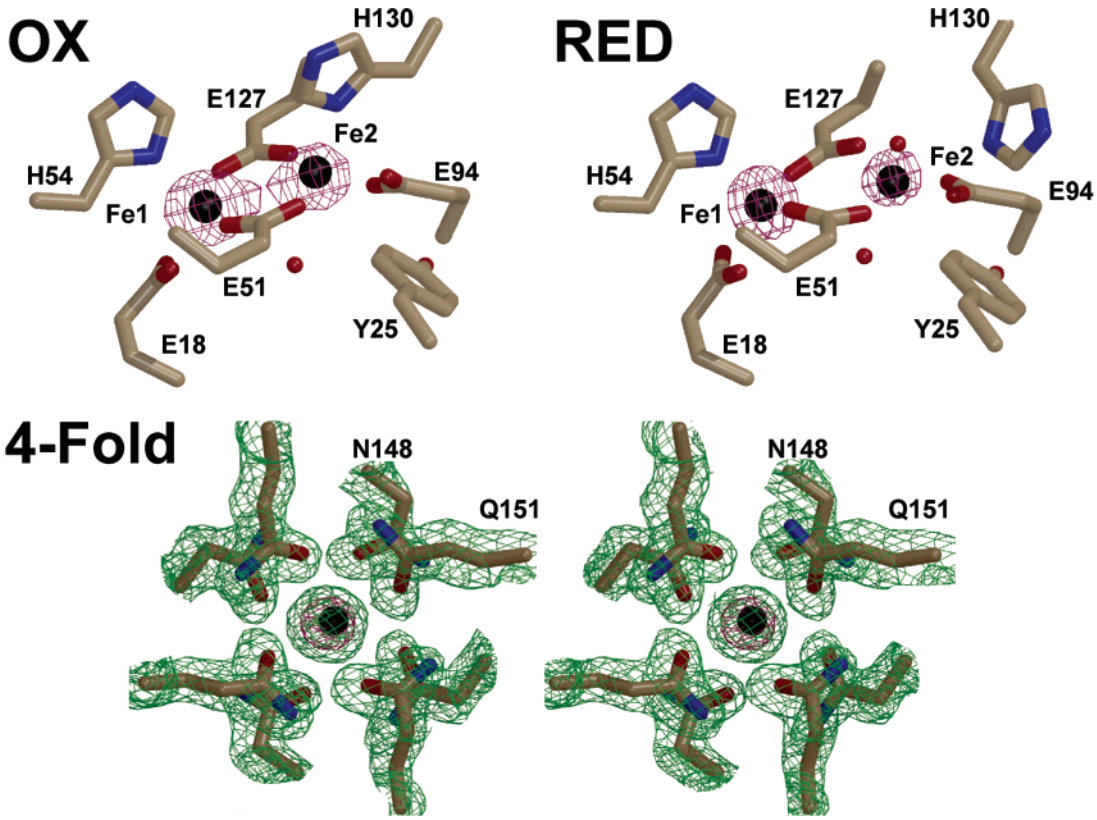

FIGURE 3: Comparison of the anomalous signal observed at the ferroxidase site and the four-fold pore. Model and anomalous density (purple cage) contoured at 16σ for the oxidized (OX) and anaerobic dithionite-treated (RED) AvBF data. Panel 4-FOLD is a wall-eyed stereoview of the anaerobic dithionite-treated model, the $2F_o - F_c$ composite omit map (green cage) contoured at 1σ generated with the simulated annealing protocol, and anomalous density (purple cage) contoured at 16σ for the four-fold pore of the anaerobic dithionite-treated data. For clarity, N148 and Q151 are labeled for only one of the monomers.

intersubunit salt bridge. In AvBF, this involves residues E109 and R117. Therefore, while redox-dependent signaling along helix D may be important in both bacterial and mammalian ferritins, ion transport across the three-fold pore in bacterioferritins seems less likely.

Iron Anomalous Signal and the Four-Fold Pore. The application of MAD phasing in the structure determination allows unequivocal identification of the positions of iron atoms in the asymmetric unit. In our case, anomalous data were collected for both the oxidized and anaerobic dithinoite-treated protein. The anomalous signal for the iron atoms of the ferroxidase site in both of the models is shown in Figure 3 (panels OX and RED, respectively) as well as for the iron atom at the four-fold pore. For the latter, there are a total of two sites in the asymmetric unit (six sites for the entire 24-monomer sphere).

In Figure 3, the anomalous signal comes from data collected at the peak wavelength (1.739 Å). Data collected at lower energy (i.e., >1.7392 Å) resulted in a sharp decrease in the magnitude of the anomalous signal, consistent with the assignment of this signal to iron. If the anomalous signal at the four-fold pour was in fact Ba, as modeled by Liu et al., we would expect to see a larger anomalous signal at the Fe edge (i.e., 1.7403 Å). Moreover, a Ba atom would also significantly improve the phasing statistics (Table 1), and in fact the phasing power of the iron sites used for initially generating maps is actually somewhat lower than that observed for other enzymes containing diiron sites within a four-helix bundle motif (*37*). The latter observation may in fact be due to the difficulty in actually measuring the iron edge in these crystals. This is especially important since iron is found in four different environments (i.e., heme, ferroxidase site, four-fold pore, and mineral core). Specifically, since the *A. vinelandii* cells were grown for more than 24 h prior to enzyme isolation, the bacterioferritin should contain a partially mineralized core of at least 600−1000 Fe atoms (*26*). Although these iron atoms will be disordered and not visible in the electron density, they will dominate the fluorescence scan when one is determining how to set up the MAD experiment.

The observation of higher *B* factors for the second iron atom of the ferroxidase site (iron bound by H130 in the oxidized state) is also consistent with the observation that the corresponding anomalous signal being slightly weaker. This observation is even more pronounced in the reduced data where the side chain of H130 has moved away from the iron atom (Figure 3, panel RED, Fe2). These observations are consistent with the iron site of the reduced protein being approximately 80% occupied. In contrast to the thick hydrophobic properties of the four-fold pore in the ferritins from higher organisms, the four-fold pore of the bacterioferritins is considerably thinner, typically consisting of only two layers of polar side chains. Several ions have been identified in both the three- and four-fold pores (*20*, *22*, *24*, *38*) of the bacterioferritins, and although it has been proposed to serve as a selectivity filter, an iron atom has never been observed at the four-fold pore. In contrast to previous work, we clearly see an iron anomalous signal at the four-fold pore in both the oxidized and reduced data. The anomalous signal for the anaerobic dithionite-treated crystals is shown in Figure

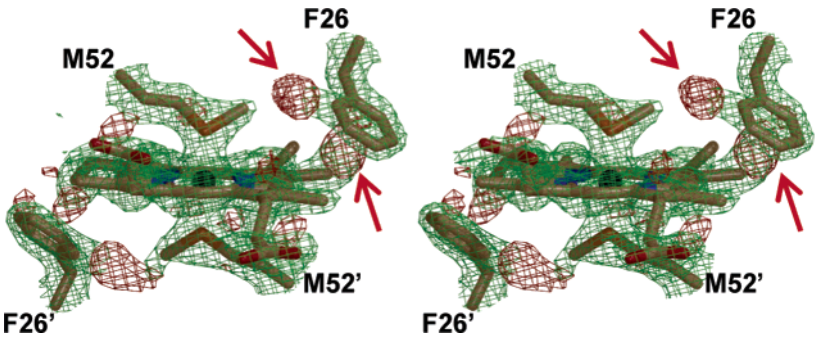

FIGURE 4: Model, composite omit map, and difference map for the heme binding site in the reduced structure. Wall-eyed stereoview of the model, $F_o - F_c$ difference map (red cage), and $2F_o - F_c$ composite omit map (green cage) generated with the simulated annealing protocol. The difference map is contoured at 3σ, while the composite omit map is contoured at 1σ.

3 (panel 4-FOLD). No additional density is observed in the difference maps when iron is modeled in this position. Moreover, the *B* factors (20.79 and 21.09) for iron atoms at each of the two different four-fold positions in the asymmetric unit are similar to the *B* factors for their ligating oxygen atoms (N148 and Q151, averages of 18.37 and 19.68, respectively). These *B* factors are also similar to those of the iron atoms in the full-occupancy position of the ferroxidase site (average of 23.15). Notably, the *B* factors for both the oxidized and reduced models are the lowest in the region of the four-fold pore, suggesting that this region of the structure has the least thermal motion. The iron atom is bound between two polar layers formed by the side chains of residues Q151 (inner layer) and N148 (outer layer). In the data for the reduced form, the iron atom is positioned within the eight oxygen atoms from the side chains of Q151 and N148 such that it is slightly close to the inner layer formed by Q151 (Figure 3). The average iron−ϵ-oxygen distance on the inner side is 2.89 Å, with the longest distance being 2.91 Å, while the average iron−ϵ-oxygen distance for the outer layer is 2.93 Å, with the longest distance measured at 3.02 Å. Finally, some movement is also observed in other residues around the four-fold pore that are conserved in the bacterioferritins, specifically, residues S152 (inner side) and E147 (outer side). Some movement of E155 and E38 (both on the inner side of the protein shell) is also observed upon reduction. The observation of an iron ion at the four-fold pore in AvBF is consistent with the hypothesis presented by Liu et al. (*24*), who suggested that this pore may serve as a selective filter for iron access. However, several distinct differences in the method of protein preparation may provide clues to explain the differences seen at the four-fold pore (H. L. Liu et al. modeled a Ba atom due to excess electron density). First, our protein was prepared under aerobic conditions in less than 24 h by a two-step procedure that essentially involved the isolation of the *A. vinelandii* chromosomal DNA (with AvBF bound) under low-salt conditions. Sodium chloride (800 mM) is then used to liberate the AvBF from precipitated DNA, and the soluble protein is subjected to gel filtration. Liu et al. reported that they were isolating and trying to crystallize a Cr-containing nitrogenase iron protein (Fe protein) when they accidentally observed the AvBF crystals. While the details of how the Cr-containing Fe protein was prepared were not clear, it is clear that significant amounts of AvBF must have copurified with the Fe protein. The purification of nitrogenase Fe protein is substantially longer (typically 3 days) and is performed under anaerobic and reducing conditions. In any case, the lack of iron at the four-fold pore and the ferroxidase site observed by Liu et al. (*24*) is consistent with the idea that iron release requires reduction.

Heme Binding in AvBF. The heme binding pocket in all of the bacterioferritins is symmetrical because it is found at a perfect two-fold rotation axis between two equivalent monomers. It is therefore not surprising that in the structures of several bacterioferritins, the heme has been proposed to adopt several conformations (*22*, *23*). In contrast to what was previously reported by Liu et al., two pieces of evidence presented here suggest that this also is the case for AvBF. First, phases for both the oxidized and anaerobic dithionite-treated data sets were obtained by MAD phasing using space group *R*32. In this space group, two of the heme molecules are found on a crystallographic two-fold axis, suggesting that density surrounding these iron positions is symmetrical. Given the nonsymmetrical structure of the *b*-type heme, this is impossible, and we changed to space group *R*3 so that all (now four) heme groups could be accurately modeled. In contrast to the very clean density that was observed around the iron atom at the four-fold pore, the electron density at the heme binding sites was more difficult to model. In particular, the heme groups, originally placed on the crystallographic two-fold axis of space group *R*32, revealed significant peaks in the difference maps. The model, composite omit map, and difference map for one of these heme sites are shown in Figure 4. Evidence for movement and/or possible multiple conformations of the heme group is apparent with the positive peaks observed in the difference maps. In addition to the positive peaks that can be associated with the potential vinyl groups of a "flipped" heme, density near F26 can also be observed and is consistent with the movement of the heme and this proximal residue.

Mg Ions and the "B" Pore. In the data published by Macedo et al. on the structure of DdBF, a pore distinct from the three- and four-fold symmetry pores was noted and termed the B site (*23*). This pore is visible in our data for both the oxidized and anaerobic dithionite-treated AvBF and clearly contains octahedral Mg ions ligated by water molecules (Figure 5A). Similar to what was reported for DdBF, a concentrated negative charge is observed in this area due to the presence of E135, D132, and D139 from one monomer, as well as D34 and E66 from adjacent monomers. While the exact role of this pore is uncertain, it is clear that this pore is sufficiently large to accommodate an iron atom. It should be noted that magnesium not only is found in the growth media but also is a requirement for crystallization and is present at 200 mM in the mother liquor.

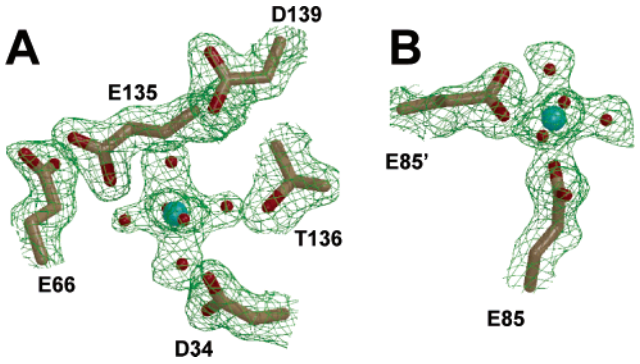

FIGURE 5: Model and composite omit map for key magnesium binding sites in *A. vinelandii* bacterioferritin. The binding of magnesium to the B site (A) and on the surface of the protein shell (B) is shown. Magnesium, oxygen, and carbon atoms are colored cyan, red, and brown, respectively. For clarity, only the side chains of the amino acids are labeled. In panel A, residues E135, T136, and D139 are from the C monomer, residue D34 is from the E monomer, and E66 is from the D monomer. In panel B, E85 is from monomer D of one protein sphere and E85′ comes from a symmetry-related monomer of another protein sphere in the unit cell.

The magnesium requirement for crystallization is clearly due to the presence of an additional magnesium site involving the side chain of E85 from the monomer of one sphere and the same side chain from another monomer in an entirely different sphere (Figure 5B). A similar phenomenon was also observed with cadmium in the structure of mouse L-chain ferritin (*39*, *40*).

Conclusions. The redox biochemistry of ferritins and the diiron carboxylate protein family is of central importance to the respective functions of specific enzymes. The observation of redox-dependent conformational changes in several key residues clearly supports the hypothesis for a gating mechanism of iron entry and/or exit at the ferroxidase site in AvBF. Whether this is a common theme in other bacterioferritins remains to be further investigated. The observation of iron atoms at the four-fold pore is novel and further supports the hypothesis that these pores may serve as selectivity filters for iron in AvBF.

The combination of the selectivity filter and a carefully gated iron mineralization mechanism may explain why the formation of peroxide is not observed during this process in AvBF. Essentially, since we see evidence for communication between the ferroxidase site and the three-fold pore in AvBF (a potential site for mineralization), activation of ferrous iron for mineralization might only occur when the activated intermediate can readily be transferred to a growing mineral core at the three-fold axis. However, certain nonspecific interactions cannot be ruled out. In particular, the iron ligation and solvent exposure of the ferroxidase site are significantly different in mammalian ferritins and do vary to a certain extent in the bacterioferritins. This variation may allow reaction intermediates to escape or other molecules in the solvent to react at the ferroxidase site and account for these mechanistic differences as suggested by Bunker et al. (*15*).

In summary, a model for iron mineralization in bacterioferritin that seems to be developing supports a mechanism by which ferrous iron enters through the four-fold pore and reacts with O_2 at the ferroxidase site to produce an activated iron-oxo species. This species is then transferred to the three-fold axis where it is added to a growing mineral core. The precise atomic details of this process and the exact role of the B site remain to be established.

REFERENCES

1. Liu, X., and Theil, E. C. (2005) Ferritins: Dynamic management of biological iron and oxygen chemistry, *Acc. Chem. Res. 38*, 167−75.
2. Carrondo, M. A. (2003) Ferritins, iron uptake and storage from the bacterioferritin viewpoint, *EMBO J. 22*, 1959−68.
3. Ferreira, C., Bucchini, D., Martin, M. E., Levi, S., Arosio, P., Grandchamp, B., and Beaumont, C. (2000) Early embryonic lethality of H ferritin gene deletion in mice, *J. Biol. Chem. 275*, 3021−4.
4. Zhao, G., Ceci, P., Ilari, A., Giangiacomo, L., Laue, T. M., Chiancone, E., and Chasteen, N. D. (2002) Iron and hydrogen peroxide detoxification properties of DNA-binding protein from starved cells. A ferritin-like DNA-binding protein of *Escherichia coli*, *J. Biol. Chem. 277*, 27689−96.
5. Ilari, A., Stefanini, S., Chiancone, E., and Tsernoglou, D. (2000) The dodecameric ferritin from *Listeria innocua* contains a novel intersubunit iron-binding site, *Nat. Struct. Biol. 7*, 38−43.
6. Zanotti, G., Papinutto, E., Dundon, W., Battistutta, R., Seveso, M., Giudice, G., Rappuoli, R., and Montecucco, C. (2002) Structure of the neutrophil-activating protein from *Helicobacter pylori*, *J. Mol. Biol. 323*, 125−30.
7. Ceci, P., Ilari, A., Falvo, E., and Chiancone, E. (2003) The Dps protein of *Agrobacterium tumefaciens* does not bind to DNA but protects it toward oxidative cleavage: X-ray crystal structure, iron binding, and hydroxyl-radical scavenging properties, *J. Biol. Chem. 278*, 20319−26.
8. Wang, G., Olczak, A. A., Walton, J. P., and Maier, R. J. (2005) Contribution of the *Helicobacter pylori* thiol peroxidase bacterioferritin comigratory protein to oxidative stress resistance and host colonization, *Infect. Immun. 73*, 378−84.
9. Lumppio, H. L., Shenvi, N. V., Summers, A. O., Voordouw, G., and Kurtz, D. M., Jr. (2001) Rubrerythrin and rubredoxin oxidoreductase in *Desulfovibrio vulgaris*: A novel oxidative stress protection system, *J. Bacteriol. 183*, 101−8.
10. Kurtz, D. M., Jr. (1999) Oxygen-carrying proteins: Three solutions to a common problem, *Essays Biochem. 34*, 85−100.
11. Waldo, G. S., and Theil, E. C. (1993) Formation of iron(III)-tyrosinate is the fastest reaction observed in ferritin, *Biochemistry 32*, 13262−9.
12. Waldo, G. S., Ling, J., Sanders-Loehr, J., and Theil, E. C. (1993) Formation of an Fe(III)-tyrosinate complex during biomineralization of H-subunit ferritin, *Science 259*, 796−8.
13. Sun, S., Arosio, P., Levi, S., and Chasteen, N. D. (1993) Ferroxidase kinetics of human liver apoferritin, recombinant H-chain apoferritin, and site-directed mutants, *Biochemistry 32*, 9362−9.
14. Yang, X., Chen-Barrett, Y., Arosio, P., and Chasteen, N. D. (1998) Reaction paths of iron oxidation and hydrolysis in horse spleen and recombinant human ferritins, *Biochemistry 37*, 9743−50.
15. Bunker, J., Lowry, T., Davis, G., Zhang, B., Brosnahan, D., Lindsay, S., Costen, R., Choi, S., Arosio, P., and Watt, G. D. (2005) Kinetic studies of iron deposition catalyzed by recombinant human liver heavy and light ferritins and *Azotobacter vinelandii* bacterioferritin using O_2 and H_2O_2 as oxidants, *Biophys. Chem. 114*, 235−44.
16. Xu, B., and Chasteen, N. D. (1991) Iron oxidation chemistry in ferritin. Increasing Fe/O_2 stoichiometry during core formation, *J. Biol. Chem. 266*, 19965−70.
17. Yang, X., Le Brun, N. E., Thomson, A. J., Moore, G. R., and Chasteen, N. D. (2000) The iron oxidation and hydrolysis chemistry of *Escherichia coli* bacterioferritin, *Biochemistry 39*, 4915−23.
18. Yang, X., Chiancone, E., Stefanini, S., Ilari, A., and Chasteen, N. D. (2000) Iron oxidation and hydrolysis reactions of a novel ferritin from *Listeria innocua*, *Biochem. J. 349* (Part 3), 783−6.
19. Bou-Abdallah, F., Lewin, A. C., Le Brun, N. E., Moore, G. R., and Chasteen, N. D. (2002) Iron detoxification properties of *Escherichia coli* bacterioferritin. Attenuation of oxyradical chemistry, *J. Biol. Chem. 277*, 37064−9.
20. Frolow, F., Kalb, A. J., and Yariv, J. (1994) Structure of a unique two-fold symmetric haem-binding site, *Nat. Struct. Biol. 1*, 453−60.

21. Dautant, A., Meyer, J. B., Yariv, J., Precigoux, G., Sweet, R. M., Kalb, A. J., and Frolow, F. (1998) Structure of a monoclinic crystal from of cyctochrome b_1 (Bacterioferritin) from *E. coli*, *Acta Crystallogr. D54* (Patt 1), 16−24.
22. Cobessi, D., Huang, L. S., Ban, M., Pon, N. G., Daldal, F., and Berry, E. A. (2002) The 2.6 Å resolution structure of *Rhodobacter capsulatus* bacterioferritin with metal-free dinuclear site and heme iron in a crystallographic 'special position', *Acta Crystallogr. D58*, 29−38.
23. Macedo, S., Romao, C. V., Mitchell, E., Matias, P. M., Liu, M. Y., Xavier, A. V., LeGall, J., Teixeira, M., Lindley, P., and Carrondo, M. A. (2003) The nature of the di-iron site in the bacterioferritin from *Desulfovibrio desulfuricans*, *Nat. Struct. Biol. 10*, 285−90.
24. Liu, H. L., Zhou, H. N., Xing, W. M., Zhao, J. F., Li, S. X., Huang, J. F., and Bi, R. C. (2004) 2.6 Å resolution crystal structure of the bacterioferritin from *Azotobacter vinelandii*, *FEBS Lett. 573*, 93−8.
25. Gupta, N., Bonomi, F., Kurtz, D. M., Jr., Ravi, N., Wang, D. L., and Huynh, B. H. (1995) Recombinant *Desulfovibrio vulgaris* rubrerythrin. Isolation and characterization of the diiron domain, *Biochemistry 34*, 3310−8.
26. Watt, G. D., Frankel, R. B., Papaefthymiou, G. C., Spartalian, K., and Stiefel, E. I. (1986) Redox Properties and Mossbauer Spectroscopy of *Azotobacter vinelandii* bacterioferritin, *Biochemistry 25*, 4330−6.
27. Schneider, T. R., and Sheldrick, G. M. (2002) Substructure solution with SHELXD, *Acta Crystallogr. D58*, 1772−9.
28. Terwilliger, T. C. (2000) Maximum-likelihood density modification, *Acta Crystallogr. D56* (Part 8), 965−72.
29. Terwilliger, T. C., and Berendzen, J. (1999) Automated MAD and MIR structure solution, *Acta Crystallogr. D55* (Part 4), 849−61.
30. Wang, B. C. (1985) Resolution of phase ambiguity in macromolecular crystallography, *Methods Enzymol. 115*, 90−112.
31. Jones, T. A., Zou, J. Y., Cowan, S. W., and Kjeldgaard, M. (1991) Improved methods for building protein models in electron density maps and the location of errors in these models, *Acta Crystallogr. A47* (Part 2), 110−9.
32. Brünger, A. T., Adams, P. D., Clore, G. M., DeLano, W. L., Gros, P., Grosse-Kunstleve, R. W., Jiang, J., Kuszewski, J., Nilges, M., Pannu, N. S., Read, R. J., Rice, L. M., Simonson, T., and Warren, G. L. (1998) Crystallography & NMR System: A New Software Suite for Macromolecular Structure Determination, *Acta Crystallogr. D54*, 905−21.
33. Yano, J., Kern, J., Irrgang, K. D., Latimer, M. J., Bergmann, U., Glatzel, P., Pushkar, Y., Biesiadka, J., Loll, B., Sauer, K., Messinger, J., Zouni, A., and Yachandra, V. K. (2005) X-ray damage to the Mn_4Ca complex in single crystals of photosystem II: A case study for metalloprotein crystallography, *Proc. Natl. Acad. Sci. U.S.A. 102*, 12047−52.
34. Jin, W., Takagi, H., Pancorbo, B., and Theil, E. C. (2001) "Opening" the ferritin pore for iron release by mutation of conserved amino acids at interhelix and loop sites, *Biochemistry 40*, 7525−32.
35. Takagi, H., Shi, D., Ha, Y., Allewell, N. M., and Theil, E. C. (1998) Localized unfolding at the junction of three ferritin subunits. A mechanism for iron release? *J. Biol. Chem. 273*, 18685−8.
36. Zeth, K., Offermann, S., Essen, L. O., and Oesterhelt, D. (2004) Iron-oxo clusters biomineralizing on protein surfaces: Structural analysis of *Halobacterium salinarum* DpsA in its low- and high-iron states, *Proc. Natl. Acad. Sci. U.S.A. 101*, 13780−5.
37. Iyer, R. B., Silaghi-Dumitrescu, R., Kurtz, D. M., Jr., and Lanzilotta, W. N. (2005) High-resolution crystal structures of *Desulfovibrio vulgaris* (Hildenborough) nigerythrin: Facile, redox-dependent iron movement, domain interface variability, and peroxidase activity in the rubrerythrins, *J. Biol. Inorg. Chem. 10*, 407−16.
38. Harrison, P. M., Hempstead, P. D., Artymiuk, P. J., and Andrews, S. C. (1998) Structure−function relationships in the ferritins, *Met. Ions Biol. Syst. 35*, 435−77.
39. Granier, T., Gallois, B., Langlois d'Estaintot, B., Dautant, A., Chevalier, J. M., Mellado, J. M., Beaumont, C., Santambrogio, P., Arosio, P., and Precigoux, G. (2001) Structure of mouse L-chain ferritin at 1.6 Å resolution, *Acta Crystallogr. D57*, 1491−7.
40. Granier, T., Langlois d'Estaintot, B., Gallois, B., Chevalier, J. M., Precigoux, G., Santambrogio, P., and Arosio, P. (2003) Structural description of the active sites of mouse L-chain ferritin at 1.2 Å resolution, *J. Biol. Inorg. Chem. 8*, 105−11.

BI060146W